Dynamic mode decomposition of GRACE satellite data

G. Libero [a], V. Ciriello [a,*], D.M. Tartakovsky [b]

[a] *Department of Civil, Chemical, Environmental and Materials Engineering, University of Bologna, Italy*
[b] *Department of Energy Science and Engineering, Stanford University, USA*

ARTICLE INFO

ABSTRACT

Advancements in satellite technology yield environmental data with ever improving spatial coverage and temporal resolution. This necessitates the development of techniques to discern actionable information from large amounts of such data. We explore the potential of dynamic mode decomposition (DMD) to discover the dynamics of spatially correlated structures present in global-scale data, specifically in observations of total water storage anomalies provided by GRACE satellite missions. Our results demonstrate that DMD enables data compression and extrapolation from a reduced set of dominant spatiotemporal structures. The accuracy of its predictions of global system dynamics is preserved in its reconstruction of local time series. These findings suggest potential uses of DMD in analysis of remote-sensing data for hydrologic applications.

1. Introduction

Climate change poses new challenges to the sustainable exploitation of water resources and requires modeling and monitoring activities to identify and design appropriate adaptation and mitigation strategies (Huggins et al., 2022; IPCC, 2023; Scanlon et al., 2023). Satellite technologies inform these activities by providing input to both physics-based and data-driven models used to analyze climate-related phenomena (Sheffield et al., 2018; Pasetto et al., 2018; Scanlon et al., 2018; Stampoulis et al., 2019; Adams et al., 2022).

Total water storage anomalies (TWSA) are data provided by the Gravity Recovery and Climate Experiment (GRACE) satellite mission and its successor, the GRACE follow-on (GRACE–FO) (Tapley et al., 2004; Landerer et al., 2020). These satellites measure Earth's gravity field variations to detect water distribution changes on the planet and draw an integrated view of how Earth's water cycle evolves in time (Watkins et al., 2015). These observations enable one to detect trends in water distribution at regional and continental scales and hypothesize correlations with climatic conditions and anthropogenic activities (Rodell et al., 2018; Thomas and Famiglietti, 2019; Rodell and Reager, 2023). Given the importance of these observations of global water distribution, many modeling studies focus on bridging the data gap between the two satellite missions (Li et al., 2020; Sun et al., 2020).

Data-driven (e.g., machine learning) methods seek to discover constitutive relationships directly from data (model's output and/or observational data), deriving data-informed and equation-free reduced-order models (ROMs) for the interpretation of complex real-world problems (Asher et al., 2015; Lu et al., 2020). ROMs are invaluable when either a large number of model simulations is required or no model is available.

Commonly employed data-driven methods include non-intrusive response surface methods (Ciriello et al., 2019; Marzadri et al., 2024), machine learning approaches such as neural networks (NN) (Qin et al., 2019; Tartakovsky and Zong, 2024), and modal-decomposition techniques (Towne et al., 2018; Taira et al., 2020). The latter class includes dynamic mode decomposition (DMD), which constructs an "optimal" linear model for a given dynamic system in the observable space via a hierarchical decomposition of complex patterns into simpler processes (Kutz et al., 2016). Like proper orthogonal decomposition (POD) (Holmes et al., 2012) and independent component analysis (Bell and Sejnowski, 1997), DMD is based on the singular value decomposition (SVD) of temporal snapshots of the dynamic system. While the other methods provide a hierarchy of modes based on spatial correlation and energy content, DMD provides a reduced set of modes consisting of spatially correlated structures with a specific temporal evolution (time dynamic). Thus, DMD can be seen as an ideal combination of a POD-like spatial dimensionality-reduction technique with Fourier transforms in time (Kutz et al., 2016). When combined with the Koopman theory (Koopman, 1931), DMD acquires some physical interpretability (Mezić, 2013; Rowley et al., 2009).

The standard DMD (sDMD) algorithm (Tu et al., 2014) returns a best-fit linear dynamical system that advances high-dimensional measurements forward in time, i.e., a linear ROM that describes the relationship between time-shifted snapshots representing the system dynamic (Kutz et al., 2016; Lu and Tartakovsky, 2020b). Several variants (Hemati et al., 2017; Wynn et al., 2013; Jovanović et al., 2014;

---

* Corresponding author.
  E-mail address: v.ciriello@unibo.it (V. Ciriello).

Lu and Tartakovsky, 2020a; Colbrook et al., 2023) have been developed to improve the performance of model reduction and to adapt the algorithm to different applications (Schmid, 2022). Among these variants, we adopt the xDMD algorithm (Lu and Tartakovsky, 2021) that supplements sDMD with a bias term to handle inhomogeneous problems. This variant extends the applicability of DMD-based ROMs to dynamical systems described by inhomogeneous partial differential equations with inhomogeneous boundary conditions. The robustness of xDMD-based ROMs of three-dimensional fluid dynamics simulations and xDMD's efficacy in reducing the data-generation cost for ensemble-based simulations are demonstrated in Libero et al. (2024b,a).

We explore the use of DMD to represent and extrapolate GRACE data. We also provide general indications of the use and suitability of this method in remote sensing for hydrologic studies. Specifically, we quantify the efficiency and accuracy of sDMD and xDMD in the reconstruction of GRACE data at the global and local scales, i.e., at different latitudes and longitudes. Our results demonstrate that DMD is an accurate and efficient method for learning the global dynamics from dominant spatiotemporal structures present in the data, and that DMD preserves its accuracy in local time series reconstruction.

The paper is organized as follows. Section 2 is devoted to the presentation of both our methodological framework and the data used in the study. Section 3 reports the results, discussed in Section 4. Section 5 provides final remarks.

2. Materials and methods

2.1. The DMD framework for dynamic processes

Data-driven regression and machine learning techniques are becoming critical to characterize dynamical systems from data. Among these techniques, DMD (Schmid, 2010; Tu et al., 2014; Kutz et al., 2016) is a powerful tool for the characterization of high-dimensional systems and can be equally used to either experimental or numerical data.

Consider a dynamical system

$$\frac{d\mathbf{x}}{dt} = \mathbf{f}(\mathbf{x}, t; \mu), \tag{1}$$

where $\mathbf{x}(t) \in \mathbb{R}^N$ is a vector representing the system state at time t, μ includes parameters of the system, and $\mathbf{f}(\cdot)$ represents the dynamics. Typically, the state $\mathbf{x}$ arises from the discretization of a PDE at a number N of spatial locations. The continuous-time dynamics in Eq. (1) may also induce a discrete-time representation deriving from the sample of the system state every Δt in time (hereinafter snapshots) so that $\mathbf{x}_k = \mathbf{x}(t_k)$, with $t_k = k\Delta t$ and $k = 1, \dots, M$. As such, we define the discrete-time flow map $\mathbf{F}_{\Delta t} : \mathbb{R}^N \to \mathbb{R}^N$, which relates $\mathbf{x}_k$ to $\mathbf{x}_{k-1}$ for any Δt as

$$\mathbf{x}_k = \mathbf{F}_{\Delta t}(\mathbf{x}_{k-1}). \tag{2}$$

Note that if the dynamics $\mathbf{f}(\mathbf{x}, t; \mu)$ in Eq. (1) is unknown, only the observations of the system state can be used to approximate the dynamics and predict the future state.

2.1.1. sDMD algorithm

Let $\mathbf{X}, \mathbf{X}' \in \mathbb{R}^{N \times M}$ denote two matrices whose columns are the vectors $\mathbf{x}_0, \dots, \mathbf{x}_{M-1}$ and $\mathbf{x}_1, \dots, \mathbf{x}_M$, respectively. The sDMD approach seeks to derive a ROM of the nonlinear dynamic system described by Eq. (1), approximating the flow map of Eq. (2) by a linear model

$$\mathbf{x}_k \approx \mathbf{A}\mathbf{x}_{k-1}. \tag{3}$$

As in general $M \ll N$, the rank of $\mathbf{A}$ is at most M, however, computing the best-fit linear operator (or its spectral decomposition) as $\mathbf{A} = \mathbf{X}'\mathbf{X}^\dagger \in \mathbb{R}^{N \times N}$ remains onerous. Hence, the truncated SVD of $\mathbf{X} = \mathbf{U}\Sigma\mathbf{V}^\top$, with rank $r < M$, is used

$$\mathbf{A} \approx \mathbf{X}'\mathbf{V}\Sigma^{-1}\mathbf{U}^\top, \tag{4}$$

where $\mathbf{U} \in \mathbb{R}^{N \times r}$, $\Sigma \in \mathbb{R}^{r \times r}$, $\mathbf{V} \in \mathbb{R}^{M \times r}$. If r is smaller than the number of nonzero singular values (i.e., the rank of $\mathbf{X}$), then the truncated SVD is a proxy of $\mathbf{X}$.

This formulation (Tu et al., 2014) generalizes the original DMD (Schmid, 2010) to a larger class of datasets, including non-sequential time series. Subsequent modifications enhance the accuracy of the original algorithm. For example, total DMD (Hemati et al., 2017) reformulates DMD as a two-stage algorithm in order to address the issue of noise-induced bias. Optimal mode decomposition (Wynn et al., 2013) generalizes sDMD by using an iterative procedure to find an optimal combination of a linear model and POD modes subspace that minimizes the system residual error. A sparsity-promoting variant of sDMD (Jovanović et al., 2014) aims to achieve a desirable trade-off between the approximation quality and the number of modes used in the approximation.

2.1.2. xDMD algorithm

Given the complexity of the GRACE dataset, we also employ xDMD (Lu and Tartakovsky, 2021) to better handle inhomogeneity of the system dynamics. The sDMD equations are modified by adding both a bias term (to cope with inhomogeneous partial differential operators) and residual learning (which is proved to be highly advantageous in deep-learning). Following Chen and Xiu (2021), xDMD approximates the temporal relationship between $\mathbf{Y} = \mathbf{X}' - \mathbf{X}$ and $\mathbf{X}$ as

$$\mathbf{y}_k \approx \mathbf{B}\mathbf{x}_{k-1} + \mathbf{b}. \tag{5}$$

Here, $[\mathbf{B} \ \mathbf{b}] = \mathbf{Y}\tilde{\mathbf{X}}^\dagger \in \mathbb{R}^{N \times N+1}$, where $\tilde{\mathbf{X}}^\top = [\mathbf{X} \ \mathbf{1}]$ and $\tilde{\mathbf{X}} \in \mathbb{R}^{N+1 \times M}$. For computational saving, the best-fit linear operator is obtained through the SVD of the matrix $\tilde{\mathbf{X}} \approx \tilde{\mathbf{U}}\tilde{\Sigma}\tilde{\mathbf{V}}^\top$ as

$$[\mathbf{B} \ \mathbf{b}] \approx \mathbf{Y}\tilde{\mathbf{V}}\tilde{\Sigma}^{-1}\tilde{\mathbf{U}}^\top, \tag{6}$$

where $\tilde{\mathbf{U}} \in \mathbb{R}^{N+1 \times r}, \tilde{\Sigma} \in \mathbb{R}^{r \times r}, \tilde{\mathbf{V}} \in \mathbb{R}^{M \times r}$. The performance of xDMD can be further improved by adapting the above mentioned algorithm optimizations for sDMD.

2.1.3. Truncation rank criteria and model assessment

Three criteria are employed to select the truncation rank of both sDMD and xDMD. The first is a hard thresholding of singular values (Gavish and Donoho, 2013) of a non-square $N \times M$ matrix:

$$r' = \min(n) : \sigma_n \leq \omega(\beta)\sigma_{\text{med}}, \tag{7}$$

where σ_n is the nth singular value of $\mathbf{X}$ (or $\tilde{\mathbf{X}}$), i.e., nth diagonal element of Σ (or $\tilde{\Sigma}$); σ_{med} is the median singular value of the data matrix; $\beta = M/N$; and

$$\omega(\beta) \simeq 0.56\beta^3 - 0.95\beta^2 + 1.82\beta + 1.43. \tag{8}$$

The second option is $r = r_{90}$, where r_{90} is the number of diagonal elements of Σ (or $\tilde{\Sigma}$) corresponding to the 90% of the cumulative energy in the SVD of $\mathbf{X}$ (or $\tilde{\mathbf{X}}$). The third one is $r = r^*$, where

$$r^* = \min(n) : \sigma_n \leq 10^{-3} \sum_{k=0}^{M-1} \sigma_k. \tag{9}$$

Starting from observations of the system evolution, we employ DMD to build a ROM for use as a surrogate model. (The use of DMD to investigate the modes and time dynamics embedded in the dataset is beyond the goal of this work). Although there are methods to evaluate the specific error linked to the notion of modal ordering and physical interpretability of the modes (Higham et al., 2018), we chose to evaluate the performance of the ROM only through the comparison between observed and simulated system states.

The difference between the state of the system predicted by the generic DMD ROM and the real snapshot at time t_k is

$$\mathbf{d}_k^\mathcal{L} = \mathbf{x}_k^\mathcal{L} - \mathbf{x}_k, \tag{10}$$

Table 1

Number of snapshots (M) and ranks considered for representation and extrapolation tests.

Task	Train	Test	r'	r_{90}	r^*	Rank($\mathbf{X}$)
Representation	$M = 196$	$M = 196$	73	79	122	195
Extrapolation	$M = 148$	$M = 48$	55	72	124	147

where $\mathcal{L}$ indicates the ROM's approximation. Hence, similarly to Lu and Tartakovsky (2021), we define the relative error at a given time as follows

$$\epsilon_k^{\mathcal{L}} = \frac{\|\mathbf{d}_k^{\mathcal{L}}\|^2}{\|\mathbf{x}_k\|^2}, \tag{11}$$

where $\| \cdot \|$ denotes vector 2-norm.

The information loss due to the truncation, which is carried out in the SVD decomposition and affects the model accuracy, is evaluated by comparing the error $\epsilon_k^{\mathcal{L}}$ associated with the different truncation options described above, considering as a reference the case $r = \text{rank}(\mathbf{X})$ (i.e., no truncation).

2.2. GRACE data

The GRACE satellite mission (Tapley et al., 2004; Watkins et al., 2015), which was in orbit from April 2002 to October 2017, and its successor, the GRACE-FO (Landerer et al., 2020), launched in 2018 and still working, take advantage of gravity field measurements, to derive information about how global water distribution evolves in time. Each mission counts a pair of orbiting satellites continuously tracking how their relative distance is affected by Earth's gravity field variations. These changes reflect mass distribution variations on Earth, primarily due to changes in water storage in hydrologic reservoirs, moving ocean, atmospheric and land ice masses, and mass exchanges between these compartments. The vertical extent of these changes is measured in centimeters of equivalent water thickness (EWT).

TWSA are derived from satellite measurements and then are freely provided to the users as global matrices of centimeters of EWT anomalies with respect to a baseline mean (Jan 2004–Dec 2009). Monthly data are available with some short-term gaps and a major interruption due to the transition between the missions. The native resolution is 3 degrees in both latitude and longitude, but a 0.5-degree scaling factor map is provided to compensate for the signal attenuation during sampling and post-processing (Wiese et al., 2016). This also acts as a mask, removing oceans and areas around the poles, where specific analyses should be considered.

For this study, the most recent GRACE mascon product (RL06.1Mv03) is downloaded from the Jet Propulsion Laboratory archive (NASA/JPL, 2023), together with the scaling factor file and a list of the months of activity of the two missions. The dataset we use collects 215 snapshots of TWSA (in cm) between April 2002 ($t = 1$) and November 2022 ($t = 248$), each one counting $N = 58908$ grid elements placed on land areas. From the entire dataset, subsets of snapshots are transformed into column vectors to build two data matrices $\mathbf{X}$ and $\mathbf{X}'$, whose correspondent columns are shifted of the same Δt, to train and test the DMD ROMs.

3. Results

We explore the accuracy, in representation and extrapolation, of a set of DMD-based ROMs obtained by truncating the SVD of the data matrix $\mathbf{X}$ at four different ranks, either $r = r'$, r_{90}, r^*, or rank($\mathbf{X}$), i.e., no truncation.

3.1. Global data representation

First, both the sDMD and xDMD algorithms are tested on the entire dataset of available snapshots. Specifically, we train the ROMs by extracting from the original dataset $M = 196$ couples of snapshots equally shifted in time by $\Delta t = 1\text{month}$ (Table 1). The ability of both algorithms to reproduce the training set is tested and quantified through the representation error $\epsilon_k^{\mathcal{L}}$ (Eq. (11)).

The curve of the cumulative energy in panel (a) of Fig. 1 shows how the informative content carried by the training data is decomposed and distributed among the elements of the SVD. By definition, the cumulative energy associated with $r = \text{rank}(\mathbf{X})$ is equal to 1, while 10% of the information is lost when r_{90} is applied; truncating at r^* keeps around 95% of the energy in this case. Since $r' \simeq r_{90}$ and the associated cumulative energy is approximately the same, in what follows we consider only the case $r = r_{90}$. In the other panels of Fig. 1, the representation error averaged over k, i.e. $\epsilon^{\mathcal{L}}$, is depicted as function of r for sDMD- (panel (b)) and xDMD- (panel (c)) based ROMs, respectively.

In Fig. 2 we compare how the error $\epsilon_k^{\mathcal{L}}$ associated with the sDMD- and xDMD-based ROMs (panels (a) and (b), respectively), truncated at r_{90}, r^* and rank($\mathbf{X}$), evolve in time.

Additionally, the representation performance of both the formulations of DMD is analyzed locally in space in Fig. 3. On the first row (panels (a) and (b)), two maps, serving as references, show the original values of TWSA provided by GRACE for $t = 124$, and 248. The differences $\mathbf{d}_k^{\mathcal{L}}$ between them and the reconstructions provided by DMD are computed through Eq. (10) and mapped in the remaining panels. Panels (c)–(d) and (e)–(f) show the results for sDMD and xDMD, respectively. Here, all the ROMs are truncated at r_{90}. Each of the four maps in panels (c)–(f) is accompanied by two curves: in the vertical graph is the mean by row of the absolute values of the mapped local differences; in the horizontal graph, the same by column, to enhance different performances in latitudes and longitudes. To each time t_k corresponds a vector of differences $\mathbf{d}_k^{\mathcal{L}}$ containing $N = 58908$ values $\mathrm{d}_k^{\mathcal{L}}$, one for each cell located on a land area in the map.

The probability distribution of $\mathrm{d}_k^{\mathcal{L}}$ is described by the histograms in Fig. 4. Each plot symmetrically refers to the corresponding map in panels (c)–(f) of Fig. 3.

3.2. Global data extrapolation

To test the performance of DMD in the extrapolation regime, the original GRACE dataset is split into a training set, counting $M = 148$ pairs of snapshots, extracted in $t = 1 \div 200$, and a test set made with the remaining 48 pairs, in $t = 201 \div 248$ (see Table 1). The first group of data is employed to train both sDMD- and xDMD-based ROMs, which are then used to predict the following states of the system. The performance is assessed by comparing the DMD predictions with the test set elements and computing the extrapolation error according to Eq. (11). Panel (a) of Fig. 5 shows the evolution in time of the extrapolation error of the sDMD-based ROM truncated at r_{90}, r^* and rank($\mathbf{X}$); panel (b) shows the same for xDMD.

Fig. 6 does the same as Fig. 3, but here the maps refer to $t = 224$ and $t = 248$, as the focus is specifically on the extrapolated part of the series ($t = 201 \div 248$). The TWSA maps provided by GRACE for $t = 224$ and $t = 248$ are plotted on the first row, in panels (a) and (b). The differences $\mathbf{d}_k^{\mathcal{L}}$ between them and the corresponding maps predicted by sDMD are on the second row (panels (c) and (d)), while the plots of the third row (panels (e) and (f)) refer to the xDMD.

The histograms in Fig. 7, symmetrically paired to the maps of panels (c)–(f) in Fig. 6, describe the probability distributions of $\mathrm{d}_k^{\mathcal{L}}$ for the extrapolation test.
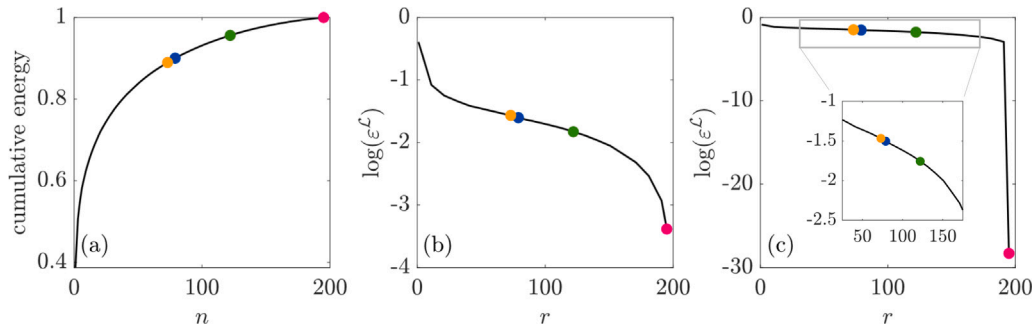
Fig. 1. (a) Cumulative energy associated with the SVD of **X** vs. the singular values number *n*. Representation error (averaged over time) $\varepsilon^{\mathcal{L}}$ of the (b) sDMD-, and (c) xDMD-based ROMs vs. *r*. In all panels, the yellow, blue, green, and red dots correspond to r', r_{90}, r^*, and rank(**X**), respectively.
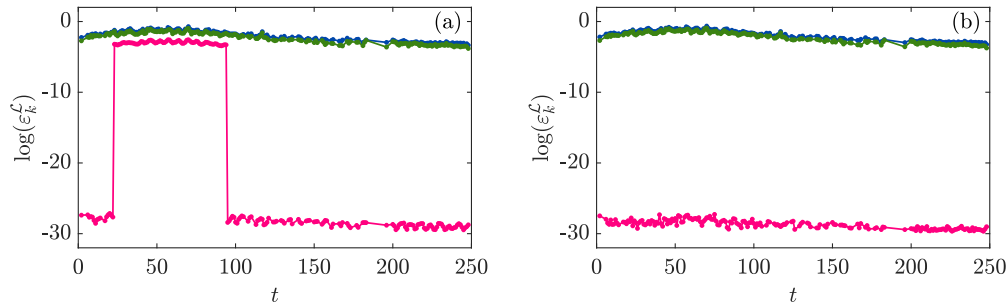
Fig. 2. Representation error $\varepsilon_k^{\mathcal{L}}$ (Eq. (11)) of the (a) sDMD- and (b) xDMD-based ROMs. In each plot different lines correspond to the ROMs with different truncation ranks: r_{90} in blue, r^* in green, and rank(**X**) in red. Dots over the lines correspond to t_k, with $k = 1, \ldots, M$ and $M = 196$ (see Table 1).

3.3. Local time series reconstruction

Fig. 8 offers a more detailed evaluation of the local performance of the DMD. For 6 points on the Planet, the time series of TWSA provided by GRACE are compared to the representations ($t \leq 200$) and extrapolations ($t > 200$) computed by the xDMD-based ROM truncated at r_{90}. Selected points are in the following basins (a) Amazon (Brazil), (b) San Joaquin (California, USA), (c) Po (Italy), (d) Hai Ho (China), (e) Roper (Australia), and (f) Nilo (Uganda).

4. Discussion

A key role in ROM efficiency is played by the selection of the truncation rank in the SVD of data matrix **X**, which should guarantee an optimal balance between predictive accuracy and data compression. This selection is typically done via experimentation, rendering the method's implementation subjective.

Fig. 1 shows that the curves of the representation error for the sDMD (panel (b)) and xDMD (panel (c)) are both steeper at the beginning, where maintaining one more single element in the SVD corresponds to a big gain in information and therefore in model accuracy. The error continues its decay slower in the central part of the curves so that truncating at r_{90} or r^* yields very similar results ($\log(\varepsilon^{\mathcal{L}}) \sim -1.6 \div -1.5$ in the first case, and $\log(\varepsilon^{\mathcal{L}}) \sim -1.8$ in the second one). The end of the curves ($r = $ rank(**X**)), instead, marks the difference between the two with a significantly higher performance of the xDMD ($\log(\varepsilon^{\mathcal{L}}) \sim -28.3$, while $\log(\varepsilon^{\mathcal{L}}) \sim -3.4$ for the sDMD under the same conditions).

Overall, our results show that r_{90}, which corresponds to about the 40% of singular values (see Table 1), assures a good balance between predictive accuracy and data compression in this case study. In general, based on our tests performed on different applications (Libero et al., 2024a), the indication is to select *r* in the range $[r_{90}, r^*]$, which allows capturing the salient features of the phenomena while excluding noise that produces overfitting and compromises the ROM performance in interpolation or extrapolation. Thus avoiding reconstructing the whole

behavior of the error as a function of *r*, which can be computationally prohibitive in some cases.

We note that sDMD and xDMD, truncating at r_{90} or r^*, yield very close performances, also locally in time, with a slight advantage for r^* (Fig. 2). Both the algorithms, for both the truncation ranks, lose accuracy in the range $t = 23 \div 94$ (passing from $\log(\varepsilon_k^{\mathcal{L}}) \sim -2.0 \div -3.5$ to $\log(\varepsilon_k^{\mathcal{L}}) \sim -1.5 \div -1.0$). In this same time window, it is noticeable the difference between the algorithms when $r = $ rank(**X**). Indeed, in the case of sDMD a significant increase of the error is shown. This time interval corresponds to months between January 2004 and December 2009, the same taken as the baseline of GRACE missions data. To analyze this behavior, we need to consider that all GRACE data are provided as anomalies with respect to the reference interval, which means that the baseline mean is subtracted from all the measurements, with the consequence that the subset of snapshots in 2004–2009 has zero mean, while the rest of the dataset has not. This peculiarity of the GRACE dataset is better interpreted by xDMD, which can count on the bias term and the residual learning (Eq. (5)) to model this behavior. However, this advantage is evident only when no truncation is applied to SVD, otherwise sDMD and xDMD return very similar performance.

To analyze the representation error locally in space, we observe in Fig. 3 for July 2012 ($t = 124$) and November 2022 ($t = 248$) the values of $d_k^{\mathcal{L}}$ over the globe for the two algorithms truncated at r_{90}. These values, together with the mean by latitude and longitude of $|d_k^{\mathcal{L}}|$, reveal that the ROMs mainly lose accuracy at higher latitudes, where the presence of perennial ice and topographic adjustments affect the accuracy of original data. However, the maps of $d_k^{\mathcal{L}}$ show the efficiency of the ROMs. Even if locally xDMD provides accentuated differences, e.g., in the South of Africa, in Siberia, or on the East Coast of North America, the spatial pattern of $d_k^{\mathcal{L}}$ is almost the same for both algorithms. The probability distributions of $d_k^{\mathcal{L}}$ in Fig. 3(c)–(f) are symmetric around zero. The probability quickly decays and is almost negligible for $|d_k^{\mathcal{L}}| > 5$, thus denoting a remarkable accuracy of the DMD reconstruction with both the ROMs for $r = r_{90}$.

Moving on to the analysis of the accuracy of the method in extrapolation, Fig. 5 confirms that truncating at r_{90} guarantees the best overall
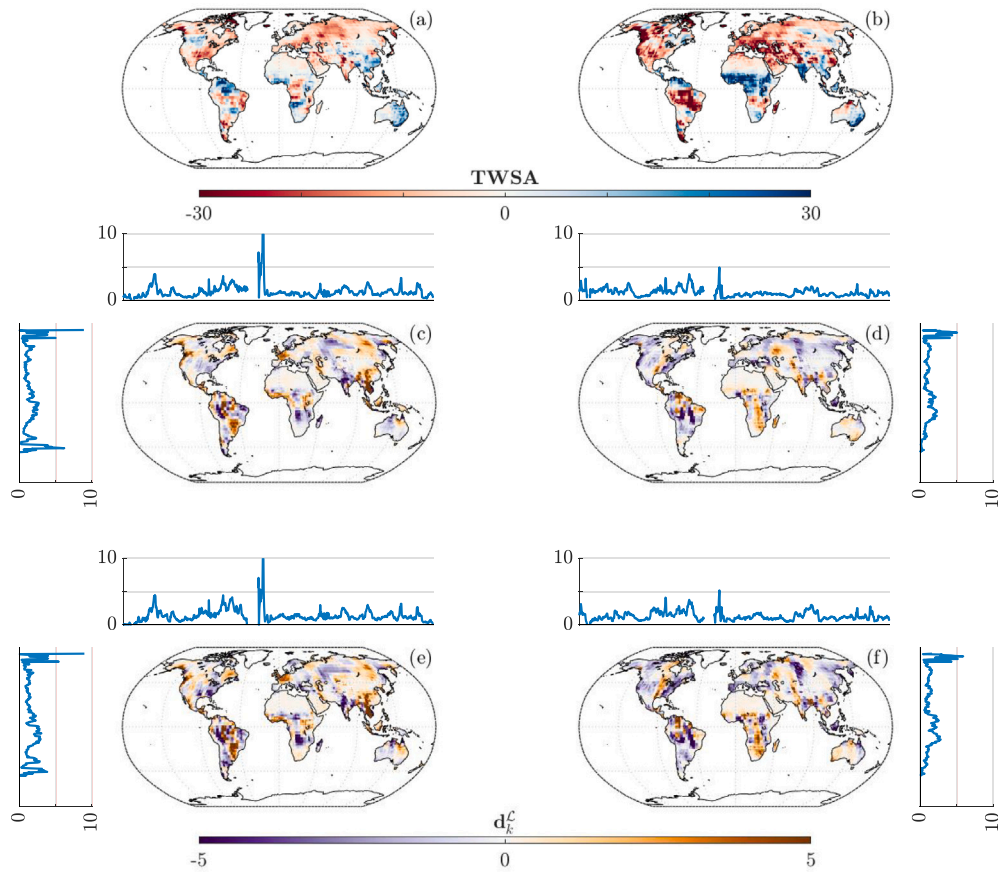
Fig. 3. Maps of TWSA (cm) provided by GRACE at (a) $t = 124$ and (b) $t = 248$ and maps of the differences $\mathbf{d}_k^{\mathcal{L}}$ (Eq. (10)) associated with the reconstructions provided by (c–d) the sDMD- and (e–f) the xDMD-based ROM, truncated at r_{90}. In panels (c–f) the curves in blue represent the mean of the absolute values of the mapped local differences by latitude (vertical) and longitude (horizontal).
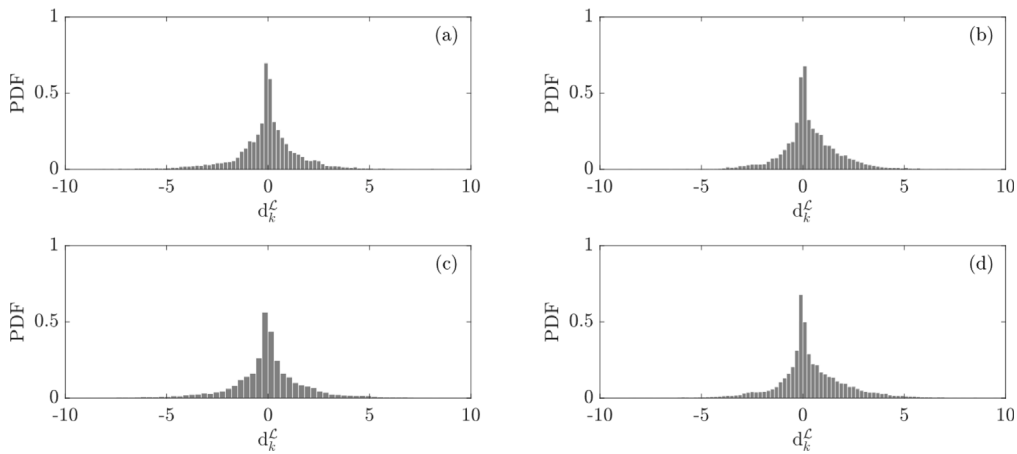
Fig. 4. Probability distribution of $\mathrm{d}_k^{\mathcal{L}}$, mapped in Fig. 3, between GRACE data for time $t = 124$ and $t = 248$ and the respective reconstructions provided by (a–b) the sDMD- and (c–d) the xDMD-based ROM, both truncated at r_{90}.

performance. Indeed, the selection of $r = \mathrm{rank}(\mathbf{X})$, which corresponds to the lowest representation error (Fig. 2), provides the worst approximation in the extrapolation regime. In general, as expected for all the machine learning methods, the ROMs provide higher errors when used to extrapolate future states of the system. Also, a slight increase of the error is noticed for $r = \mathrm{rank}(\mathbf{X})$ and r^* as we extend the number of predicted time steps. However, the ROMs return a more accurate

prediction when truncated at r_{90}, for which the error is also more stable in time, denoting the robustness of the approach, especially when xDMD is employed.

In line with these results, Fig. 6 shows that compared to the representation regime, the differences between original data and DMD predictions are higher but only a slight increase in their value is detected from November 2020 ($t = 224$) to November 2022 ($t = 248$).
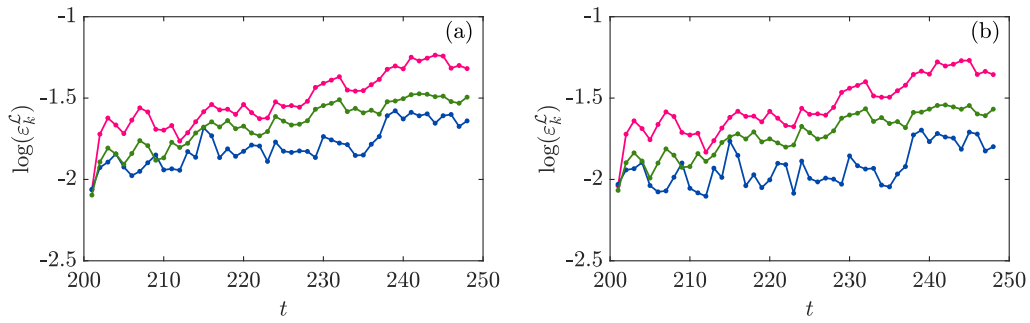
Fig. 5. Extrapolation error $\varepsilon_k^{\mathcal{L}}$ (Eq. (11)) of the (a) sDMD- and (b) the xDMD-based ROMs. In each plot different lines correspond to the ROMs with different truncation ranks: r_{90} in blue, r^* in green, and rank($\mathbf{X}$) in red. Dots over the lines correspond to t_k, with $k = 1, \ldots, M$ and $M = 48$ (see Table 1).
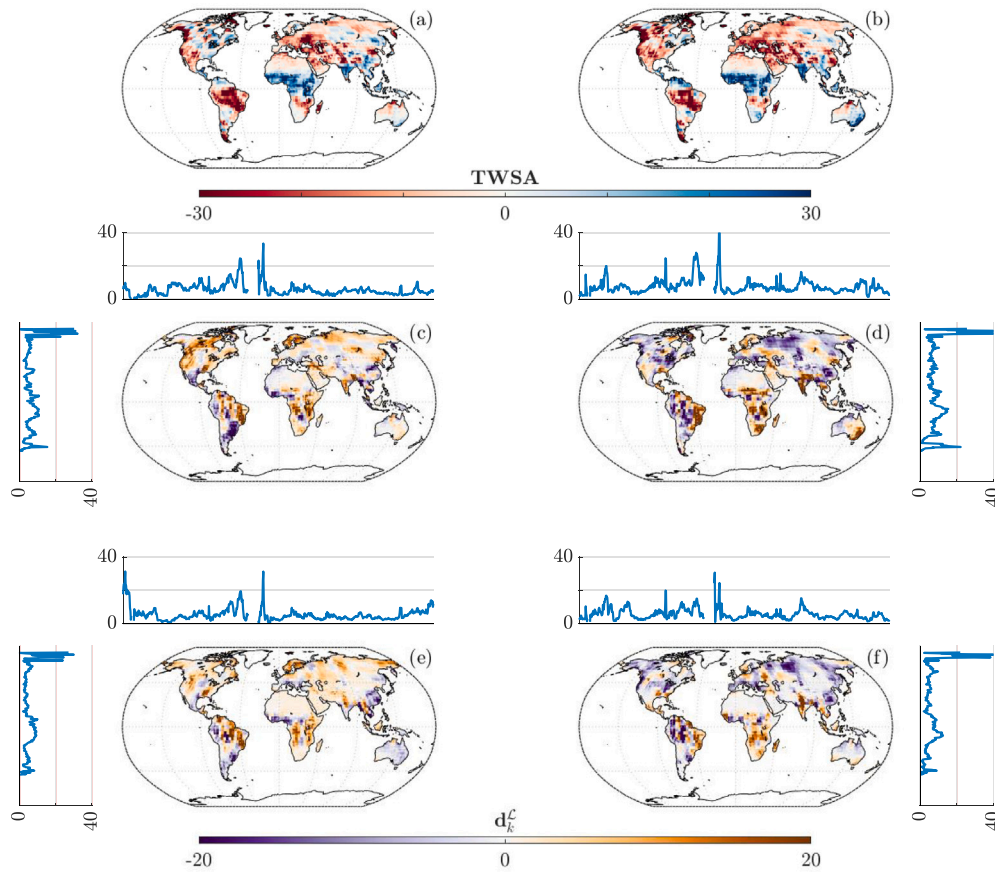

Fig. 6. Maps of TWSA (cm) provided by GRACE at (a) $t = 224$ and (b) $t = 248$ and maps of the differences $\mathbf{d}_k^{\mathcal{L}}$ (Eq. (10)) associated with the reconstructions provided by (c–d) the sDMD- and (e–f) the xDMD-based ROM, truncated at r_{90}. In panels (c–f) the curves in blue represent the mean of the absolute value of the mapped local differences by latitude (vertical) and longitude (horizontal).

The accuracy of xDMD-based ROM is better even if the general pattern of the error is nearly the same of the sDMD. The curves plotted over and next to each map confirm, as in representation, the major difficulties of the ROMs in predicting TWSA values at higher latitudes. Like for the representation test, the probability distributions of $\mathbf{d}_k^{\mathcal{L}}$ mapped in Fig. 6(c)–(f) are centered in zero and almost symmetric and not significantly affected by the time instant. However, in extrapolation, the pdf appears more sensitive to the choice of the DMD version. In the xDMD case values of $\mathbf{d}_k^{\mathcal{L}}$ close to zero are more likely to happen, according to the more narrow and high shape of the distribution, confirming the better accuracy in extrapolation of this algorithm for $r = r_{90}$.

A final analysis of representation and extrapolation tests is reproduced in Fig. 8 where we selected six locations over the globe in major basins to observe the time series reconstruction of TWSA values offered by the xDMD-based ROM truncated at r_{90}. The reconstruction is successfully performed in all the cases both in representation and in extrapolation, except for minor deviations at points (c) and (f). This result is remarkable considering that the ROM is trained with global data and tested locally, which means that with a unique data-driven model, we can reconstruct accurately local time series, thus avoiding the need to implement local approaches at each location of interest and site-specific models which do not benefit from spatial correlation information. In addition, the results are also significant because the
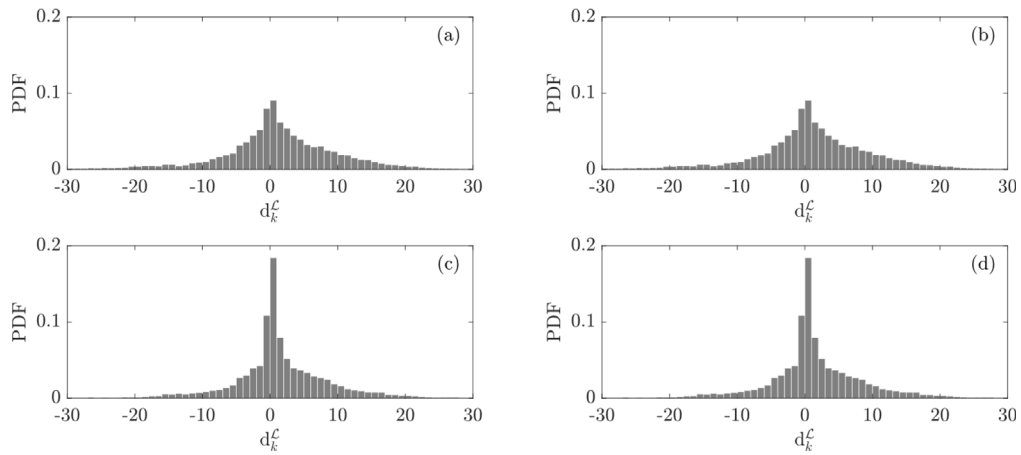
Fig. 7. Probability distribution of $d_k^{\mathcal{L}}$, mapped in Fig. 6, between GRACE data for time $t = 224$ and $t = 248$ and the respective reconstructions provided by (a–b) the sDMD- and (c–d) the xDMD-based ROM, both truncated at r_{90}.
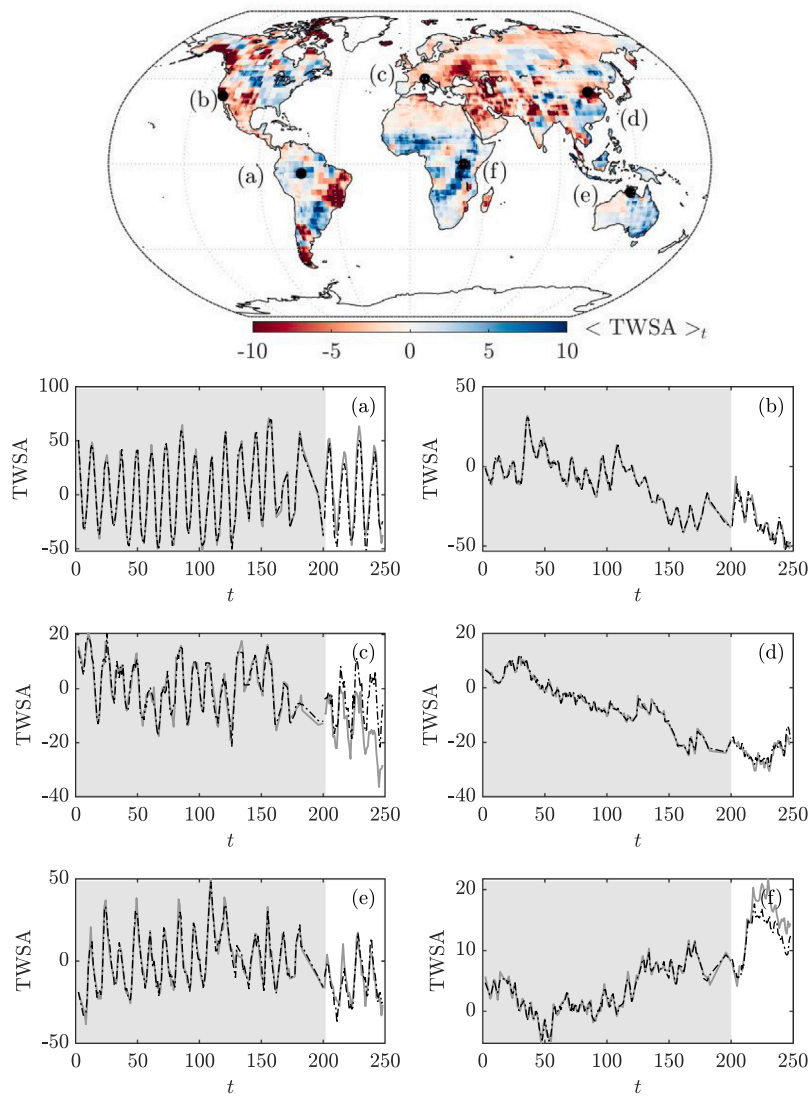

Fig. 8. (a–f) Time series of TWSA (cm) at six points as provided by GRACE (continuous gray line) and predicted by the xDMD-based ROM truncated at r_{90} (dashed line), in representation (shaded) and extrapolation regimes. The reference map represents the mean over time of TWSA in the selected range of data.

extrapolation performed is immediately after the major interruption between the two GRACE missions.

5. Conclusion

Our results indicate that DMD may have considerable implications in the field of satellite data compression and extrapolation for global hydrological data collection, management, and forecast. Indeed, the remarkable accuracy shown by the ROMs in the representation of GRACE observations unravels the possibility of using DMD for the identification of the dominant spatiotemporal structures embedded in the big dataset, which is critical for dimensionality reduction, and data storage and interpretation. At the same time, the maintenance of high standards of accuracy when used to extrapolate GRACE data, suggests the potentiality of the method for multiple purposes ranging from filling measurement gaps to short-medium forecast, which is relevant to understanding critical trends and designing mitigation strategies. We also demonstrate the benefit of dimensionality reduction in extrapolation to avoid overfitting and provide general indications on the choice of the truncation rank, which is a crucial aspect of the DMD algorithms. Based on our study, we identify the main advantages of DMD in the following points. First, based on the identification of spatially correlated structures in global-scale data and their dynamics, DMD provides an easy-to-interpret data-driven linear approximation of a dynamic process. Second, the global-scale linear approximation of the dynamic process provided by DMD allows for local time series reconstruction, thus overcoming site-specific reconstruction methods that one needs to replicate at each location of interest. Finally, the dominant spatiotemporal structures in global-scale data enable the identification of patterns and trends whose analysis for GRACE data will be developed in future studies.

CRediT authorship contribution statement

G. Libero: Writing – original draft, Software, Methodology, Investigation, Funding acquisition, Data curation, Conceptualization. **V. Ciriello:** Writing – review & editing, Supervision, Project administration, Methodology, Investigation, Funding acquisition, Conceptualization. **D.M. Tartakovsky:** Writing – review & editing, Supervision, Methodology, Funding acquisition, Conceptualization.

Declaration of competing interest

The authors declare that they have no known competing financial interests or personal relationships that could have appeared to influence the work reported in this paper.

Acknowledgments

Data availability

There are no data sharing issues since all of the numerical information is provided in the figures produced by solving the equations in the paper.

References

Adams, K.H., Reager, J.T., Rosen, P., Wiese, D.N., Farr, T.G., Rao, S., Haines, B.J., Argus, D.F., Liu, Z., Smith, R., Famiglietti, J.S., Rodell, M., 2022. Remote sensing of groundwater: Current capabilities and future directions. Water Resour. Res. 58 (10), http://dx.doi.org/10.1029/2022wr032219.

Asher, M.J., Croke, B.F.W., Jakeman, A.J., Peeters, L.J.M., 2015. A review of surrogate models and their application to groundwater modeling. Water Resour. Res. 51 (8), 5957–5973. http://dx.doi.org/10.1002/2015wr016967.

Bell, A.J., Sejnowski, T.J., 1997. The "independent components" of natural scenes are edge filters. Vis. Res. 37 (23), 3327–3338. http://dx.doi.org/10.1016/s0042-6989(97)00121-1.

Chen, Z., Xiu, D., 2021. On generalized residual network for deep learning of unknown dynamical systems. J. Comput. Phys. 438, 110362. http://dx.doi.org/10.1016/j.jcp.2021.110362.

Ciriello, V., Lauriola, I., Tartakovsky, D.M., 2019. Distribution-based global sensitivity analysis in hydrology. Water Resour. Res. 55 (11), 8708–8720. http://dx.doi.org/10.1029/2019wr025844.

Colbrook, M.J., Ayton, L.J., Szőke, M., 2023. Residual dynamic mode decomposition: robust and verified Koopmanism. J. Fluid Mech. 955, http://dx.doi.org/10.1017/jfm.2022.1052.

Gavish, M., Donoho, D.L., 2013. The optimal hard threshold for singular values is 4/sqrt(3). http://dx.doi.org/10.48550/ARXIV.1305.5870.

Hemati, M.S., Rowley, C.W., Deem, E.A., Cattafesta, L.N., 2017. De-biasing the dynamic mode decomposition for applied Koopman spectral analysis of noisy datasets. Theor. Comput. Fluid Dyn. 31 (4), 349–368. http://dx.doi.org/10.1007/s00162-017-0432-2.

Higham, J., Brevis, W., Keylock, C., 2018. Implications of the selection of a particular modal decomposition technique for the analysis of shallow flows. J. Hydraul. Res. 56 (6), 796–805. http://dx.doi.org/10.1080/00221686.2017.1419990.

Holmes, P., Lumley, J.L., Berkooz, G., Rowley, C.W., 2012. Turbulence, Coherent Structures, Dynamical Systems and Symmetry. Cambridge University Press, http://dx.doi.org/10.1017/cbo9780511919701.

Huggins, X., Gleeson, T., Kummu, M., Zipper, S.C., Wada, Y., Troy, T.J., Famiglietti, J.S., 2022. Hotspots for social and ecological impacts from freshwater stress and storage loss. Nature Commun. 13 (1), http://dx.doi.org/10.1038/s41467-022-28029-w.

IPCC, 2023. Climate Change 2022 – Impacts, Adaptation and Vulnerability. Cambridge University Press, http://dx.doi.org/10.1017/9781009325844.

Jovanović, M.R., Schmid, P.J., Nichols, J.W., 2014. Sparsity-promoting dynamic mode decomposition. Phys. Fluids 26 (2), http://dx.doi.org/10.1063/1.4863670.

Koopman, B.O., 1931. Hamiltonian systems and transformation in Hilbert space. Proc. Natl. Acad. Sci. 17 (5), 315–318. http://dx.doi.org/10.1073/pnas.17.5.315.

Kutz, J.N., Brunton, S.L., Brunton, B.W., Proctor, J.L., 2016. Dynamic Mode Decomposition. Society for Industrial and Applied Mathematics, http://dx.doi.org/10.1137/1.9781611974508.

Landerer, F.W., Flechtner, F.M., Save, H., Webb, F.H., Bandikova, T., Bertiger, W.I., Bettadpur, S.V., Byun, S.H., Dahle, C., Dobslaw, H., Fahnestock, E., Harvey, N., Kang, Z., Kruizinga, G.L.H., Loomis, B.D., McCullough, C., Murböck, M., Nagel, P., Paik, M., Pie, N., Poole, S., Strekalov, D., Tamisiea, M.E., Wang, F., Watkins, M.M., Wen, H.-Y., Wiese, D.N., Yuan, D.-N., 2020. Extending the global mass change data record: GRACE follow-on instrument and science data performance. Geophys. Res. Lett. 47 (12), http://dx.doi.org/10.1029/2020gl088306.

Li, F., Kusche, J., Rietbroek, R., Wang, Z., Forootan, E., Schulze, K., Lück, C., 2020. Comparison of data-driven techniques to reconstruct (1992–2002) and predict (2017–2018) GRACE-like gridded total water storage changes using climate inputs. Water Resour. Res. 56 (5), http://dx.doi.org/10.1029/2019wr026551.

Libero, G., Chiofalo, A., Ciriello, V., Tartakovsky, D.M., 2024a. Extended dynamic mode decomposition for model reduction in fluid dynamics simulations. Phys. Fluids 36 (6), http://dx.doi.org/10.1063/5.0207957.

Libero, G., Tartakovsky, D., Ciriello, V., 2024b. Polynomial chaos enhanced by dynamic mode decomposition for order-reduction of dynamic models. Adv. Water Resour. 186, 104677. http://dx.doi.org/10.1016/j.advwatres.2024.104677.

Lu, H., Ermakova, D., Wainwright, H.M., Zheng, L., Tartakovsky, D.M., 2020. Data-informed emulators for multi-physics simulations. http://dx.doi.org/10.48550/ARXIV.2012.15488.

Lu, H., Tartakovsky, D.M., 2020a. Lagrangian dynamic mode decomposition for construction of reduced-order models of advection-dominated phenomena. J. Comput. Phys. 407, 109229. http://dx.doi.org/10.1016/j.jcp.2020.109229.

Lu, H., Tartakovsky, D.M., 2020b. Prediction accuracy of dynamic mode decomposition. SIAM J. Sci. Comput. 42 (3), A1639–A1662. http://dx.doi.org/10.1137/19m1259948.

Lu, H., Tartakovsky, D.M., 2021. Extended dynamic mode decomposition for inhomogeneous problems. J. Comput. Phys. 444, 110550. http://dx.doi.org/10.1016/j.jcp.2021.110550.

Marzadri, A., Ciriello, V., de Barros, F.P.J., 2024. Hyporheic flows in stratified sediments: Implications on residence time distributions. Water Resour. Res. 60 (1), http://dx.doi.org/10.1029/2023wr035625.

Mezić, I., 2013. Analysis of fluid flows via spectral properties of the Koopman operator. Annu. Rev. Fluid Mech. 45 (1), 357–378. http://dx.doi.org/10.1146/annurev-fluid-011212-140652.

NASA/JPL, 2023. JPL GRACE and GRACE-FO mascon ocean, ice, and hydrology equivalent water Height Coastal resolution improvement (CRI) filtered release 06.1 version 03. http://dx.doi.org/10.5067/TEMSC-3JC63.

Pasetto, D., Arenas-Castro, S., Bustamante, J., Casagrandi, R., Chrysoulakis, N., Cord, A.F., Dittrich, A., Domingo-Marimon, C., Serafy, G.E., Karnieli, A., Kordelas, G.A., Manakos, I., Mari, L., Monteiro, A., Palazzi, E., Poursanidis, D., Rinaldo, A., Terzago, S., Ziemba, A., Ziv, G., 2018. Integration of satellite remote sensing data in ecosystem modelling at local scales: Practices and trends. In: Pettorelli, N. (Ed.), Methods Ecol. Evol. 9 (8), 1810–1821. http://dx.doi.org/10.1111/2041-210x.13018.

Qin, T., Wu, K., Xiu, D., 2019. Data driven governing equations approximation using deep neural networks. J. Comput. Phys. 395, 620–635. http://dx.doi.org/10.1016/j.jcp.2019.06.042.

Rodell, M., Famiglietti, J.S., Wiese, D.N., Reager, J.T., Beaudoing, H.K., Landerer, F.W., Lo, M.-H., 2018. Emerging trends in global freshwater availability. Nature 557 (7707), 651–659. http://dx.doi.org/10.1038/s41586-018-0123-1.

Rodell, M., Reager, J.T., 2023. Water cycle science enabled by the GRACE and GRACE-FO satellite missions. Nat. Water 1 (1), 47–59. http://dx.doi.org/10.1038/s44221-022-00005-0.

Rowley, C.W., Mezić, I., Bagheri, S., Schlatter, P., Henningson, D.S., 2009. Spectral analysis of nonlinear flows. J. Fluid Mech. 641, 115–127. http://dx.doi.org/10.1017/s0022112009992059.

Scanlon, B.R., Fakhreddine, S., Rateb, A., de Graaf, I., Famiglietti, J., Gleeson, T., Grafton, R.Q., Jobbagy, E., Kebede, S., Kolusu, S.R., Konikow, L.F., Long, D., Mekonnen, M., Schmied, H.M., Mukherjee, A., MacDonald, A., Reedy, R.C., Shamsudduha, M., Simmons, C.T., Sun, A., Taylor, R.G., Villholth, K.G., Vörösmarty, C.J., Zheng, C., 2023. Global water resources and the role of groundwater in a resilient water future. Nat. Rev. Earth Environ. 4 (2), 87–101. http://dx.doi.org/10.1038/s43017-022-00378-6.

Scanlon, B.R., Zhang, Z., Save, H., Sun, A.Y., Müller Schmied, H., van Beek, L.P.H., Wiese, D.N., Wada, Y., Long, D., Reedy, R.C., Longuevergne, L., Döll, P., Bierkens, M.F.P., 2018. Global models underestimate large decadal declining and rising water storage trends relative to GRACE satellite data. Proc. Natl. Acad. Sci. 115 (6), http://dx.doi.org/10.1073/pnas.1704665115.

Schmid, P.J., 2010. Dynamic mode decomposition of numerical and experimental data. J. Fluid Mech. 656, 5–28. http://dx.doi.org/10.1017/s0022112010001217.

Schmid, P.J., 2022. Dynamic mode decomposition and its variants. Annu. Rev. Fluid Mech. 54 (1), 225–254. http://dx.doi.org/10.1146/annurev-fluid-030121-015835.

Sheffield, J., Wood, E.F., Pan, M., Beck, H., Coccia, G., Serrat-Capdevila, A., Verbist, K., 2018. Satellite remote sensing for water resources management: Potential for supporting sustainable development in data-poor regions. Water Resour. Res. 54 (12), 9724–9758. http://dx.doi.org/10.1029/2017wr022437.

Stampoulis, D., Reager, J.T., David, C.H., Andreadis, K.M., Famiglietti, J.S., Farr, T.G., Trangsrud, A.R., Basilio, R.R., Sabo, J.L., Osterman, G.B., Lundgren, P.R., Liu, Z., 2019. Model-data fusion of hydrologic simulations and GRACE terrestrial water storage observations to estimate changes in water table depth. Adv. Water Resour. 128, 13–27. http://dx.doi.org/10.1016/j.advwatres.2019.04.004.

Sun, Z., Long, D., Yang, W., Li, X., Pan, Y., 2020. Reconstruction of GRACE data on changes in total water storage over the global land surface and 60 basins. Water Resour. Res. 56 (4), http://dx.doi.org/10.1029/2019wr026250.

Taira, K., Hemati, M.S., Brunton, S.L., Sun, Y., Duraisamy, K., Bagheri, S., Dawson, S.T.M., Yeh, C.-A., 2020. Modal analysis of fluid flows: Applications and outlook. AIAA J. 58 (3), 998–1022. http://dx.doi.org/10.2514/1.j058462.

Tapley, B.D., Bettadpur, S., Ries, J.C., Thompson, P.F., Watkins, M.M., 2004. GRACE measurements of mass variability in the earth system. Science 305 (5683), 503–505. http://dx.doi.org/10.1126/science.1099192.

Tartakovsky, A.M., Zong, Y., 2024. Physics-informed machine learning method with space-time Karhunen-Loève expansions for forward and inverse partial differential equations. J. Comput. Phys. 499, 112723. http://dx.doi.org/10.1016/j.jcp.2023.112723.

Thomas, B.F., Famiglietti, J.S., 2019. Identifying climate-induced groundwater depletion in GRACE observations. Sci. Rep. 9 (1), http://dx.doi.org/10.1038/s41598-019-40155-y.

Towne, A., Schmidt, O.T., Colonius, T., 2018. Spectral proper orthogonal decomposition and its relationship to dynamic mode decomposition and resolvent analysis. J. Fluid Mech. 847, 821–867. http://dx.doi.org/10.1017/jfm.2018.283.

Tu, J.H., Rowley, C.W., Luchtenburg, D.M., Brunton, S.L., Kutz, J.N., 2014. On dynamic mode decomposition: Theory and applications. J. Comput. Dyn. 1 (2), 391–421. http://dx.doi.org/10.3934/jcd.2014.1.391.

Watkins, M.M., Wiese, D.N., Yuan, D.-N., Boening, C., Landerer, F.W., 2015. Improved methods for observing earth's time variable mass distribution with GRACE using spherical cap mascons. J. Geophys. Res.: Solid Earth 120 (4), 2648–2671. http://dx.doi.org/10.1002/2014jb011547.

Wiese, D.N., Landerer, F.W., Watkins, M.M., 2016. Quantifying and reducing leakage errors in the JPL RL05M GRACE mascon solution. Water Resour. Res. 52 (9), 7490–7502. http://dx.doi.org/10.1002/2016wr019344.

Wynn, A., Pearson, D.S., Ganapathisubramani, B., Goulart, P.J., 2013. Optimal mode decomposition for unsteady flows. J. Fluid Mech. 733, 473–503. http://dx.doi.org/10.1017/jfm.2013.426.